

Article

Photothermal-Assisted Photocatalytic Degradation of Tetracycline in Seawater Based on the Black g-C₃N₄ Nanosheets with Cyano Group Defects

Loic Jiresse Nguetsa Kuate ^{1,†}, Zhouze Chen ^{2,†}, Jialin Lu ¹, Huabing Wen ¹, Feng Guo ^{1,*} and Weilong Shi ^{2,*} ¹ School of Energy and Power, Jiangsu University of Science and Technology, Zhenjiang 212003, China² School of Material Science and Engineering, Jiangsu University of Science and Technology, Zhenjiang 212003, China

* Correspondence: gfeng0105@126.com (F.G.); shiwl@just.edu.cn (W.S.)

† These authors contributed equally to this work.

Abstract: As a broad-spectrum antibiotic, tetracycline (TC) has been continually detected in soil and seawater environments, which poses a great threat to the ecological environment and human health. Herein, a black graphitic carbon nitride (CN-B) photocatalyst was synthesized by the one-step calcination method of urea and phloxine B for the degradation of tetracycline TC in seawater under visible light irradiation. The experimental results showed that the photocatalytic degradation rate of optimal CN-B-0.1 for TC degradation was 92% at room temperature within 2 h, which was 1.3 times that of pure CN (69%). This excellent photocatalytic degradation performance stems from the following factors: (i) ultrathin nanosheet thickness reduces the charge transfer distance; (ii) the cyanogen defect promotes photogenerated carriers' separation; (iii) and the photothermal effect of CN-B increases the reaction temperature and enhances the photocatalytic activity. This study provides new insight into the design of photocatalysts for the photothermal-assisted photocatalytic degradation of antibiotic pollutants.

Keywords: photothermal-assisted; black g-C₃N₄; photocatalytic; degradation; cyano group defects



Citation: Nguetsa Kuate, L.J.; Chen, Z.; Lu, J.; Wen, H.; Guo, F.; Shi, W. Photothermal-Assisted Photocatalytic Degradation of Tetracycline in Seawater Based on the Black g-C₃N₄ Nanosheets with Cyano Group Defects. *Catalysts* **2023**, *13*, 1147. <https://doi.org/10.3390/catal13071147>

Academic Editor: Kangle Lv

Received: 13 July 2023

Revised: 22 July 2023

Accepted: 23 July 2023

Published: 24 July 2023



Copyright: © 2023 by the authors. Licensee MDPI, Basel, Switzerland. This article is an open access article distributed under the terms and conditions of the Creative Commons Attribution (CC BY) license (<https://creativecommons.org/licenses/by/4.0/>).

1. Introduction

In the past half a century, the rapid development of the mariculture industry has led to an increase in human demand for seafood. Many mariculture sites in coastal areas have been used to breed all kinds of seafood, and the bacteria in seawater are prone to the outbreak of infectious diseases in the aquaculture water bodies, endangering social health [1–4]. Tetracycline (TC), a commonly used broad-spectrum antibiotic to prevent infectious diseases and treat bacterial infections, can be widely used to eliminate pathogenic bacteria and viruses from seawater [5–7]. However, due to the strong toxicity of TC molecules, it is easy to discharge living organisms through urine or feces, polluting water bodies, causing great harm to the seawater environment and organisms, and causing many adverse effects such as bacterial drug resistance and biological toxicity [8,9].

In recent years, researchers have used Fenton oxidation, biological treatment, adsorption, and membrane separation to remove antibiotics from seawater [10–12]. Unfortunately, the above methods have high energy consumption, low removal efficiency, and high cost, which limits their practical application [13,14]. In contrast, photocatalysis is an advanced oxidation technology with low consumption, strong oxidation capacity, and high mineralization rate, which can directly use photocatalyst to absorb solar energy and produce active substances to effectively remove various kinds of low-concentration pollutants in seawater [15,16]. Among the many photocatalytic materials, graphitic carbon nitride (g-C₃N₄) is a two-dimensional (2D) layered nanosheets composed of carbon and nitrogen atoms, which has attracted wide attention due to its unique electronic band structure, excellent

optical and electronic properties, easy preparation, and high stability [17–20]. Nevertheless, the photocatalytic activity of $g\text{-C}_3\text{N}_4$ is limited by its inherent defects, including poor visible light absorption ($\lambda < 450\text{ nm}$), high electron–hole pair recombination rate, and slow charge migration rate [21–23]. In order to address these problems, various strategies have been developed to enhance the photocatalytic activity of the original $g\text{-C}_3\text{N}_4$, such as heterojunction construction, element doping, morphological control, etc. [24–26]. Among them, the introduction of cyano group defects in $g\text{-C}_3\text{N}_4$ can promote visible light absorption, and photo-generation electron–hole separation is considered an effective method to improve photocatalytic activity [27]. For example, Hu et al. prepared a $\text{BaCN-C}_3\text{N}_4$ photocatalyst that promotes visible light absorption and higher photocatalytic activity due to the presence of Ba^{2+} , which promotes partial ring-opening through heptazine rings leading to cyano group defects production [28]. However, due to the low ambient temperature and photon utilization rate, the photocatalytic degradation efficiency of photocatalysts is still low. Fortunately, the construction of the photothermal-assisted photocatalytic degradation system can increase the temperature in the reaction system through the photothermal effect of the photothermal material itself, thus accelerating the chemical reaction kinetics on the surface of the photocatalyst, promoting the transfer of photogenerated charge, and improving the photocatalytic degradation activity [29]. For instance, Yang et al. synthesized core–shell $\text{CoTiO}_3\text{@MnO}_2$ photocatalyst photothermal catalyst, which can show excellent TC degradation performance under light irradiation due to the broad-spectrum absorption and photothermal effect of MnO_2 that can promote the charge separation [30]. Similarly, Wang et al. reported the development of a photothermal-assisted photocatalytic system using graphene oxide as a photothermal substrate and $g\text{-C}_3\text{N}_4$ as a photocatalyst, which exhibited excellent stability and reusability for the degradation of antibiotics in wastewater treatment [31]. However, most of the above-mentioned researches on photothermal-assisted photocatalysis is realized by combining photothermal materials, which often has the disadvantages of a complex preparation process, poor stability, and high cost [32,33]. Considering this, it is of great significance to design an ultrathin $g\text{-C}_3\text{N}_4$ nanosheet with its own photothermal effect for the photothermal-assisted photocatalytic degradation of antibiotics.

Herein, the black carbon nitride (CN-B) photocatalysts were constructed by adding Phloxine B to the process of conventional urea preparation carbon nitride as well as using a one-step calcination method to achieve photothermal-assisted photocatalytic degradation of TC in simulated seawater under visible light irradiation. Our results exhibit that the ultrathin nanosheet thickness of CN-B reduces the charge transfer distance, and the introduction of Phloxine B leads to cyano group defects to promote the photogenerated charge transfer and make it have a strong thermal effect to improve the temperature of the reaction system and the photocatalytic activity.

2. Results and Discussion

Scanning electron microscopy (SEM) was used to observe the morphology of the as-prepared photocatalysts. As given in Figure 1a,b, the SEM images of pure CN and CN-B-0.1 photocatalysts showed small morphological differences, both of which are stacked nanosheet structures. Furthermore, the microstructure and elemental composition of CN and CN-B-0.1 were analyzed by transmission electron microscopy (TEM). As can be seen from Figure 1c,d, the thickness of CN-B-0.1 nanosheet is about 12–18 nm, indicating that the introduction of phloxine B during the process of synthesis can not only maintain the nanosheet structure of pure CN but also the ultrathin nanosheet thickness can shorten the charge transfer distance, which is more conducive to improve the photocatalytic activity. In addition, in order to further explore the elements of the as-prepared CN-B photocatalyst, the element mapping images (Figure 1e), energy dispersive X-ray spectra (EDX, Figure S1), and element composition analysis based on X-ray photoelectron spectroscopy (XPS) measurements (Table S1) presented the existence of the corresponding elements of C, N, O, and Na.

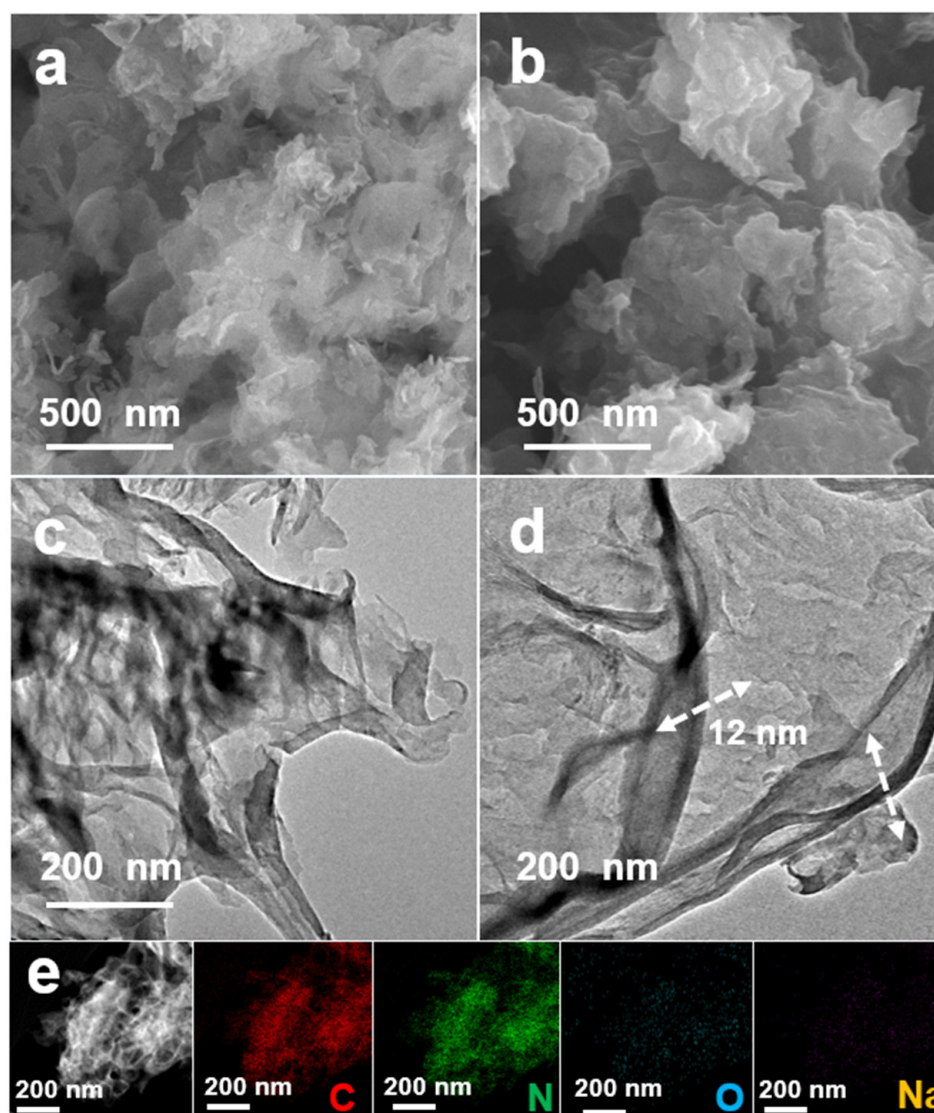


Figure 1. (a,b) SEM images of CN and CN-B-0.1. (c,d) TEM images of CN and CN-B-0.1. (e) Elemental mapping images of CN-B-0.1.

The X-ray diffraction (XRD) patterns of as-prepared CN and CN-B samples are given in Figure 2a. For the original CN sample, two distinct characteristic diffraction peaks were observed, and the first peak located at 13.2° corresponds to the (001) plane structure, specifically representing the arrangement of tris-triazine units (with the lattice of 6.76 Å) within the network of g- C_3N_4 [34,35], while the second peak situated at 27.5° is associated with the (002) plane, indicating the periodic accumulation of carbon nitride nanosheets along the c-axis [36,37]. Furthermore, compared with the XRD pattern of pure CN, the (001) peak intensity of the CN-B photocatalyst gradually decreased with the increase in the phloxine B content in the precursor, indicating a periodic disruption of the planar structure [38]. In addition, the (002) crystal plane diffraction peaks for CN-B photocatalysts exhibit slight blue shifts due to the strengthening of the interface interaction between CN-B nanosheets, decreasing the layer spacing [39,40]. The functional groups of the synthesized samples were further determined using Fourier transform infrared spectroscopy (FT-IR). Figure 2b presents the FT-IR spectra of CN-B photocatalysts are consistent with the typical vibration modes of CN, indicating that the functional group structure of CN was not significantly changed after addition of phloxine B in the precursor. Typical absorption bands located at $1200\text{--}1700\text{ cm}^{-1}$ represent the stretching mode of unique aromatic CN heterocycles, while the broadband in the $3000\text{--}3500\text{ cm}^{-1}$ range may interact with stretched

vibrations of the O-H and N-H bonds adsorbed on the CN surface [41,42]. The peak signal at 810 cm^{-1} is thought to be caused by the characteristic stretching vibration peak of the triazine unit in CN [43,44]. Another interesting finding was that a new peak was observed at 2170 cm^{-1} of the CN-B photocatalyst, caused by the tensile vibration of the cyano groups ($\text{C}\equiv\text{N}$) generated by the catalytic pyrolysis on the CN surface during the calcination of urea and phloxine B [45,46].

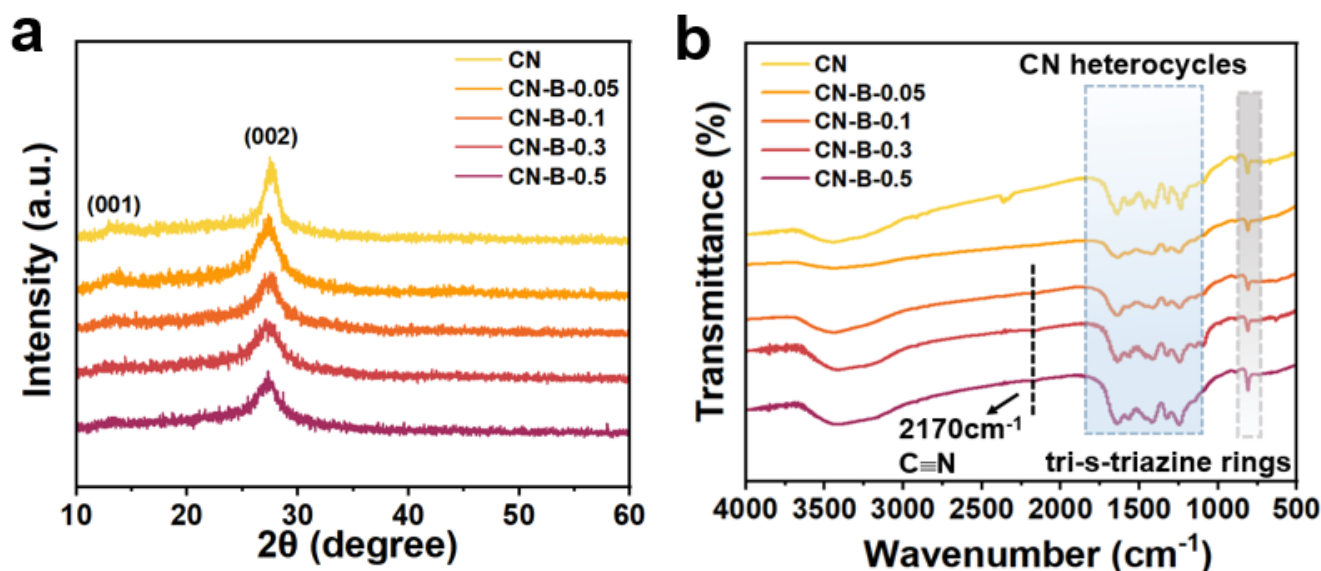


Figure 2. (a) XRD patterns and (b) FT-IR spectra of CN and CN-B photocatalysts.

The chemical composition and state of as-prepared CN and CN-B samples were revealed by XPS analysis. From the XPS survey spectra in Figure 3a, it can be observed that the CN-B-0.1 photocatalyst not only presents the C 1s, N 1s, and O 1s elements of the original CN but also detects additional Na 1s elements, which perfectly matches the results of EDX spectrum and element mapping images. Moreover, a small amount of the O element can be attributed to the adsorbed water on the CN surface, while the trace amount of the Na element may be caused by the low content of phloxine B in the photocatalyst. Compared with pure CN, CN-B-0.1 possesses a higher C atom ratio, which may be due to the increase in C content caused by the addition of phloxine B during the preparation process, resulting in an increase in the C/N atomic ratio (Table S1). As disclosed in Figure 3b, the high-resolution C1s spectrum of the CN-B-0.1 photocatalyst can be fitted to the three prominent peaks at 284.8, 285.9, and 288.2 eV, which correspond to C-C, C-N-H, and C-N=C, respectively [47,48]. The three peaks of the high-resolution N 1s spectrum of CN-B-0.1 in Figure 3c at 398.8, 399.6, and 400.8 eV are attributed to the triazine ring (C-N=C, N_{2c}), nitrogen N-(C)₃ group, and N-H bond, respectively [49,50]. For the high-resolution O 1s spectrum, CN-B-0.1 has two peaks at binding energies 532.0 and 533.4 eV (Figure 3d), which can be attributed to the C=O and C-O-H bonds [51,52]. Additionally, as presented in Figure S2, compared with pure CN, the peak of CN-B-0.1 photocatalyst at 1071.4 eV corresponds to Na 1s element [53,54]. In summary, it is evident that the positions of the C1s, N 1s, and O 1s peaks on the CN-B photocatalyst have undergone a slight shift compared to CN, indicating that the physical environment of the internal structure of CN could be changed, which affects electron transfer in the CN network to a certain extent [55,56].

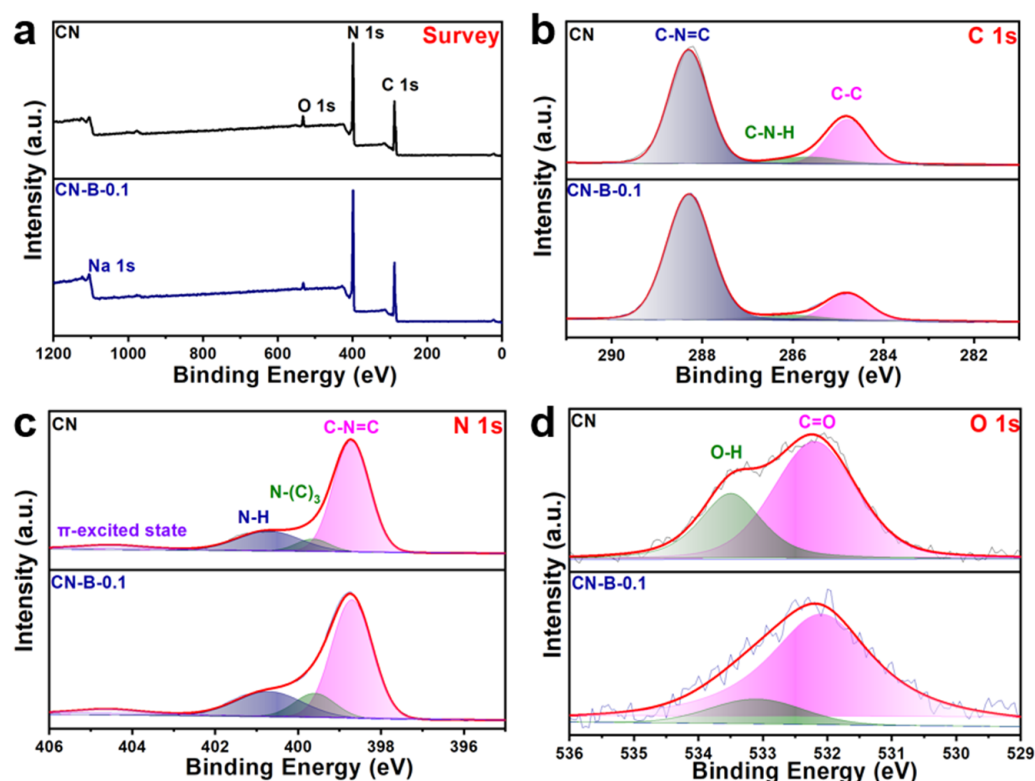


Figure 3. (a) XPS survey spectra and high-resolution XPS spectra of (b) C 1s, (c) N 1s, and (d) O 1s for CN and CN-B-0.1 photocatalysts.

The optical properties of the synthesized samples were characterized by UV-vis diffuse reflection spectra (DRS) at the absorption wavelength range of 300–800 nm. As presented in Figure 4a, pure CN exhibits the characteristic absorption pattern common in organic semiconductors, with a gap absorption of about 450 nm near the absorption edge [7,57,58]. For the CN-B photocatalysts, the absorption edge exhibits a significant red shift, increasing from 450 to 600 nm, indicating the reduced band gap and increase in visible light absorption in the visible region compared with CN-B photocatalysts. Figure S3 exhibits a digital photo of the as-prepared samples; the pure CN is pale yellow, while as the precursor increases the contents of phloxine B, the color of the CN-B photocatalyst gradually changes black, thus enhancing the absorption of visible light. In addition, the band gap values of as-prepared CN and CN-B samples were studied by using the Tauc function $(\alpha h\nu)^2 = A(h\nu - E_g)$ [59], and the corresponding bandgaps (E_g) of pure CN and different proportions of CN-B photocatalysts are given in Figure 4b. In order to further insights into the band structures of CN and CN-B, the flat band potentials (E_{fb}) of CN and CN-B-0.1 were analyzed by Mott–Schottky (M-S) measurement at tested the frequencies of 800, 1000, and 1200 Hz, respectively. As can be seen from Figure 4c, the E_{fb} of CN and CN-B-0.1 are -0.72 and -0.62 V vs. reversible hydrogen electrode (RHE), respectively, indicating that the CN-B exhibits the more negative conduction band (CB) position, thereby enhancing the photocatalytic redox ability [60,61]. Based on the position of flat band potentials and the equation of $E_{VB} = E_{CB} + E_g$, the valence band (VB) of CN and CN-B-0.1 photocatalyst is calculated to be 2.07 and 2.01 eV, respectively, and the corresponding band structure diagrams were summarized in Figure 4d.

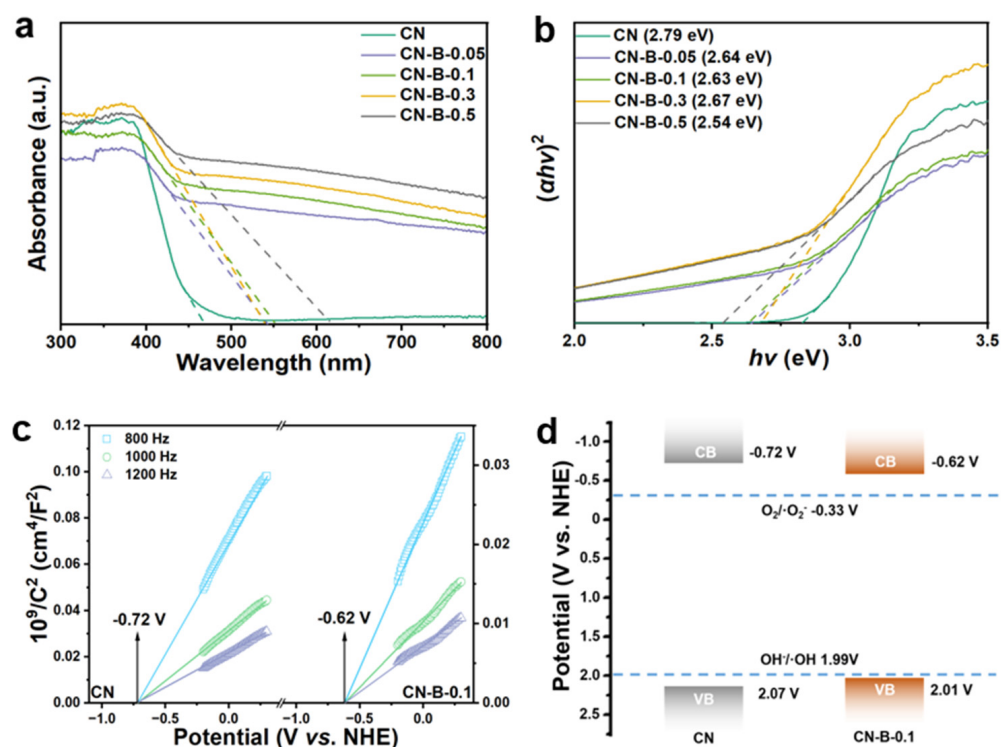


Figure 4. (a) UV-vis DRS of as-prepared photocatalysts. (b) Measured band gap values of pure CN and CN-B samples. (c) Mott-Schottky plots. (d) Energy diagrams of CN and CN-B-0.1 photocatalysts.

In order to evaluate the photocatalytic degradation efficiency of the as-prepared photocatalyst, the photocatalytic degradation experiment was carried out in simulated seawater with TC (30 mg/L) as the target pollutant under visible light irradiation. Before the photocatalytic reaction, the mixture of TC and photocatalysts was vigorously stirred without light for 30 min to ensure the adsorption-desorption equilibrium. As presented in Figure 5a, pure CN degraded only 69% of TC within 2 h under visible light radiation in simulated seawater, while the degradation rates of CN-B-0.05, CN-B-0.1, CN-B-0.3, and CN-B-0.5 were 89.4%, 91.7%, 90.9%, and 90.7%, respectively. Based on the above results, a certain amount of cyano group defect can promote photogenerated electron migration and improve the photocatalytic degradation activity of CN, while the excessive cyano group defect may lead to new photogenerated carrier recombination centers, reduce the production of active substances and thus CN-B-0.1 shows the highest photocatalytic degradation efficiency [40]. In addition, Table S2 and Figure S4 compare the performance of different materials for TC degradation reported in the literature, revealing that CN-B-0.1 photocatalyst has excellent photocatalytic degradation activity. The pseudo-first-order kinetic model was also used to fit the TC photocatalytic degradation kinetic curve and corresponding kinetic constants of the as-prepared photocatalysts (Figure 5b,c). The apparent rate constant (k) of CN-B-0.1 is 0.0242 min^{-1} , which is 2.44 times that of pure CN (0.0099 min^{-1}). Additionally, considering that the stability of the photocatalyst is one of the key factors in practical application, four continuous experiments of CN-B-0.1 photocatalytic TC degradation in simulated seawater were carried out. It is worth mentioning that CN-B-0.1 photocatalyst still maintained 90% TC degradation efficiency after four cycles of TC degradation experiment (Figure 5d), indicating that the CN-B-0.1 photocatalyst possesses superior stability. The O 1s XPS spectrum of the CN-B-0.1 photocatalyst did not remarkably changed after the photocatalysis, demonstrating that the structural stability of the CN-B-0.1 photocatalyst is well maintained (Figure S5).

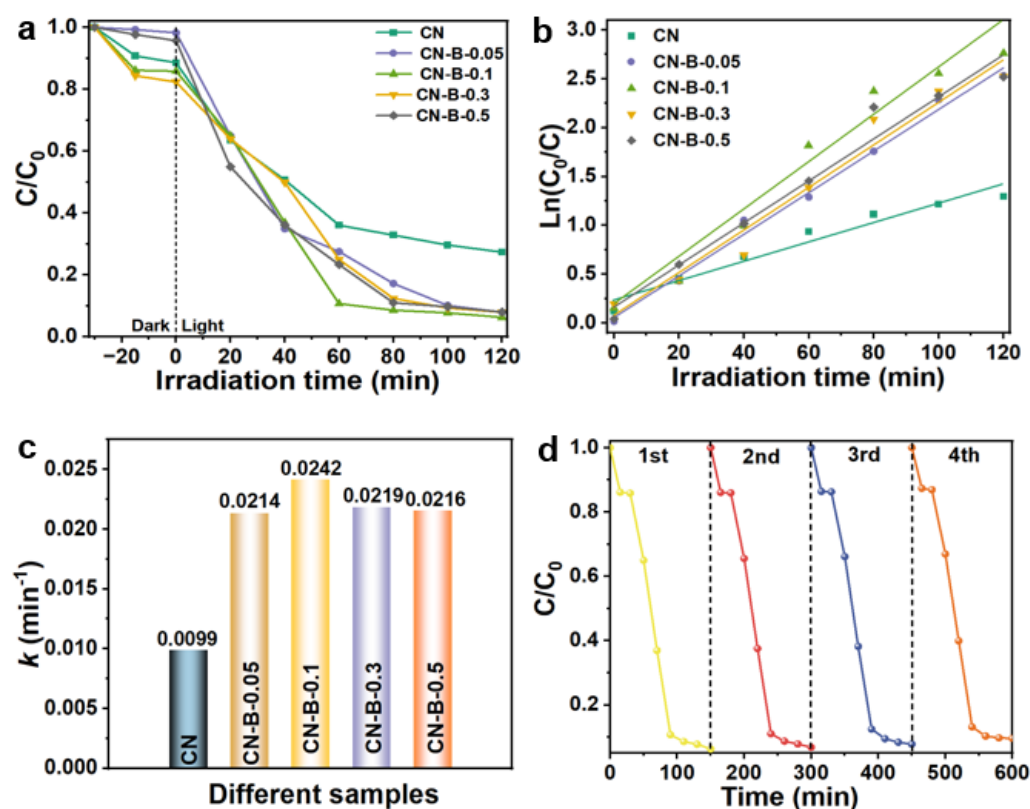


Figure 5. (a) Photocatalytic TC degradation activity of as-prepared samples in simulated seawater. (b,c) The pseudo-first-order degradation kinetic curves and corresponding degradation rate constants of as-prepared samples. (d) Four cycles of experiments for photocatalysis degradation of TC over CN-B-0.1 photocatalyst.

In order to reveal the contribution of the introduction of phloxine B precursor for the enhanced photocatalytic degradation activity, CN and CN-B-0.1 photocatalyst powders were irradiated for 150 s using a 300 W Xenon lamp, while surface temperature measurements were recorded at 30 s intervals using an infrared thermal camera. The temperature changes in CN and CN-B-0.1 photocatalysts are given in Figure 6a,b, where the temperature of CN-B-0.1 rapidly increases from 27.7 °C to 71.6 °C and remains stable, which is higher than that of pure CN (44.1 °C). This is because the introduction of phloxine B precursor deepens the CN color, prompting the photothermal effect of CN-B. Under the action of the photothermal effect, low-energy visible photons can be effectively converted into heat energy to achieve efficient photocatalytic degradation of TC, and thus the photothermal conversion efficiency of CN-B-0.1 photocatalyst (Figure 6c) was further investigated. When the entire system reaches equilibrium, the calculated time constant of CN-B-0.1 photocatalyst is 279.47 S, and the corresponding photothermal conversion efficiency (η) is 88.06%, further proving that CN-B-0.1 photocatalyst can quickly and efficiently convert light into heat energy, further accelerating the charge separation and transfer, and enhancing the photocatalytic activity. Based on the above analysis, the photocatalytic degradation activity of CN-B-1 photocatalyst was tested at different temperatures (5 °C, 10 °C, and room temperature (RT)) by controlling the reaction temperature through a circulating condensate device system. As presented in Figure 6d, pristine CN has a certain temperature sensitivity, the degradation rate decreases with the decrease in temperature, and the degradation rate reaches 69% at RT condition. In addition, the photocatalytic degradation rate of CN-B-0.1 was positively correlated with temperature, and the photocatalytic degradation rate reached 92% at the same time, indicating that the introduction of phloxine B precursor can enhance the photocatalytic degradation activity of CN by synergistic reaction of photothermal effect. Under the action of photothermal-assisted photocatalytic degradation, the

degradation kinetic curves and kinetic constants of pure CN and CN-B-0.1 photocatalysts conform to the pseudo-first-order rate equation (Figure 6e,f). The apparent rate constant k (min^{-1}) value of CN-B-0.1 photocatalyst at different temperatures (5 °C, 10 °C, and RT) is 0.005, 0.007, and 0.024 min^{-1} , which is 2.5, 1.75, and 2.4 times that of pure CN (0.002, 0.004, and 0.010 min^{-1}), respectively, indicating that increased temperature can accelerate the photocatalytic degradation rate constant and improve the photocatalytic activity. Correspondingly, photoelectrochemical characterizations at different temperatures were tested to investigate the role of photothermal effects on the catalysts' carrier dynamics. As presented in Figure 6g, at the same temperature, CN-B-0.1 RT exhibited a lower PL signal compared with pure CN due to the higher photon-generated carrier separation rate of CN-B enabled by the introduction of cyano group defects. The PL signal of CN-B-0.1 decreased significantly with increasing temperature, indicating that increasing temperature can further improve the charge separation efficiency [62–64]. In Figure 6h, CN-B-0.1 exhibited a high photocurrent response intensity, which proves the strong electron transfer capability of the modified photocatalyst [65,66]. As the ambient temperature increases, the photocurrent response intensity of CN-B-0.1 increases, which further indicates that the higher temperature further promotes electron migration and transfer, thus improving the photocatalytic production activity. For the electrochemical impedance spectrum (EIS) plots in Figure 6i, the arc radius of the CN-B-0.1 sample is less than CN and decreases as the ambient temperature increases, which again demonstrates the promotion of the cyanogen defect and the photothermal effect on electron transfer [67–69].

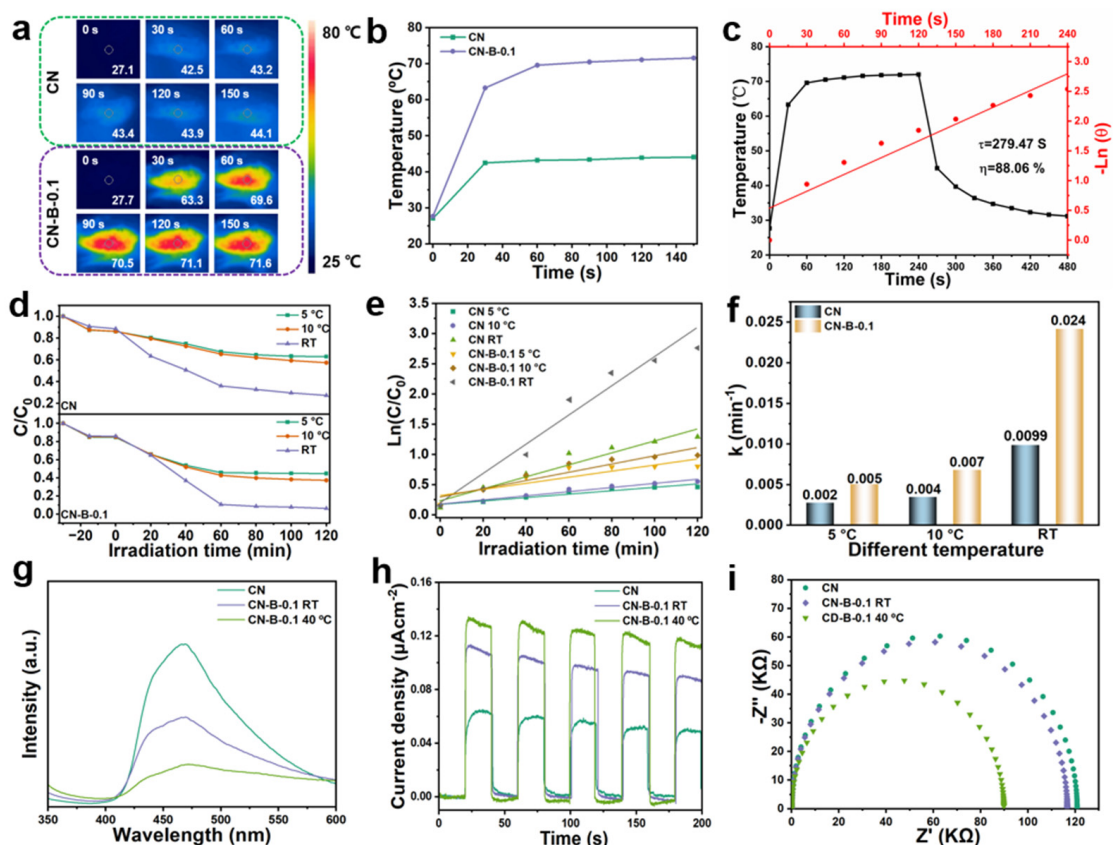


Figure 6. (a) Photothermal infrared thermal images and (b) corresponding temperature curves of CN and CN-B-0.1 in simulated seawater. (c) Temperature and photothermal conversion efficiency of CN-B-0.1 photocatalyst. (d) Photocatalytic TC degradation activity of CN and CN-B-0.1 in simulated seawater at different temperatures. (e,f) The corresponding pseudo-first-order degradation kinetic curves and kinetic constants. (g) PL spectra. (h) Transient photocurrent response curves. (i) EIS plots of pristine CN and CN-B-0.1 at RT and 40 °C.

In order to determine the main reactive radical species responsible for the photocatalytic degradation TC for the CN-B system, corresponding free radical scavenging experiments were performed [70,71]. The scavengers of 1,4-Benzoquinone (BQ), triethanolamine (TEOA), and isopropanol (IPA) were used to quench superoxide radicals ($\bullet\text{O}_2^-$), holes (h^+), and hydroxy radicals ($\bullet\text{OH}$), respectively. As presented in Figure 7a,b, after adding BQ, the final degradation efficiency of TC was effectively inhibited, indicating that $\bullet\text{O}_2^-$ radicals were the main free active radicals in the CN-B system. It is worth noting that when TEOA was added, the degradation efficiency of TC was reduced, indicating that h^+ played a secondary role in the degradation process.

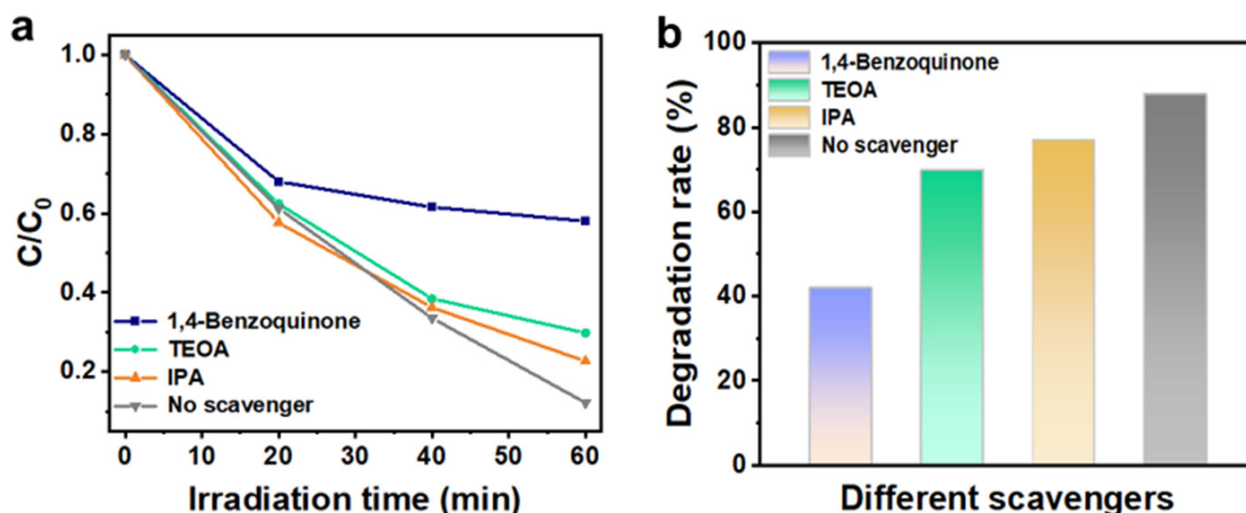
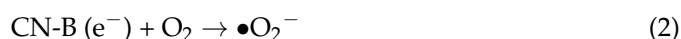
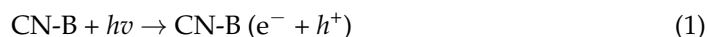


Figure 7. (a) Degradation curves and (b) corresponding degradation rate of CN-B-0.1 as the photocatalyst by adding different free radical trapping agents.

Based on the above experimental results, a possible mechanism of photothermal-assisted photocatalytic degradation TC by the CN-B photocatalyst under visible irradiation was proposed, as provided in Figure 8. The CN-B photocatalyst produces electrons and holes under visible light irradiation, while the high separation efficiency of photon-generated carriers is achieved due to the introduction of cyano group defects. More importantly, the introduction of the phloxine B precursor in CN-B can make the sample color darker to enhance the photocatalytic reaction temperature through the photothermal effect, thus enhancing the photocatalytic degradation activity. Specifically, according to the band structure of the photocatalyst, the electrons in the CB position of CN-B react with dissolved oxygen in the water to form a superoxide radical ($\bullet\text{O}_2^-$) ($E_0(\text{O}_2/\bullet\text{O}_2^-) = -0.33$ eV vs. NHE), while the h^+ in the VB of CN-B convert water molecules into $\bullet\text{OH}$ to degrade pollutants. Finally, $\bullet\text{O}_2^-$, h^+ and $\bullet\text{OH}$ degrade the TC into CO_2 , H_2O , etc. In conclusion, in the CN-B photocatalytic system, active free radicals can be generated in the following ways:



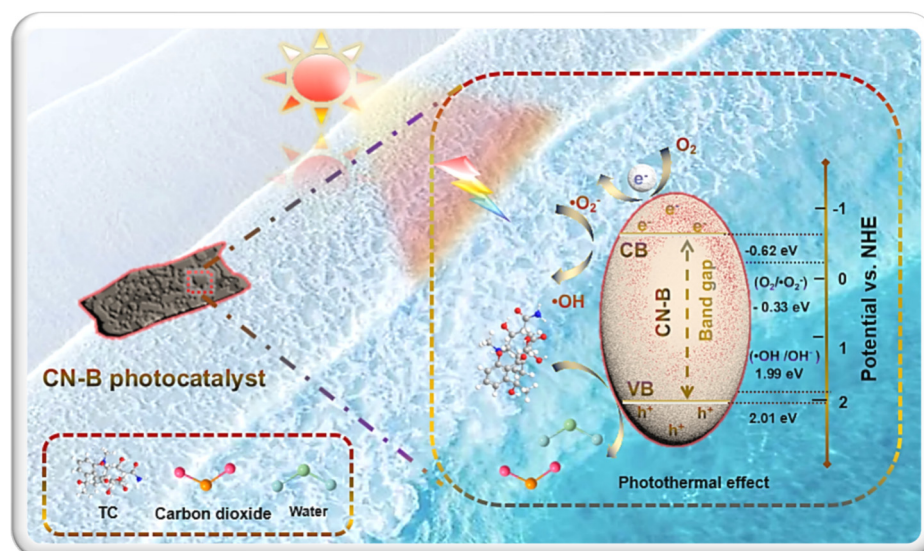


Figure 8. Possible mechanism of photothermal-assisted photocatalytic degradation TC in seawater by CN-B photocatalyst under visible light irradiation.

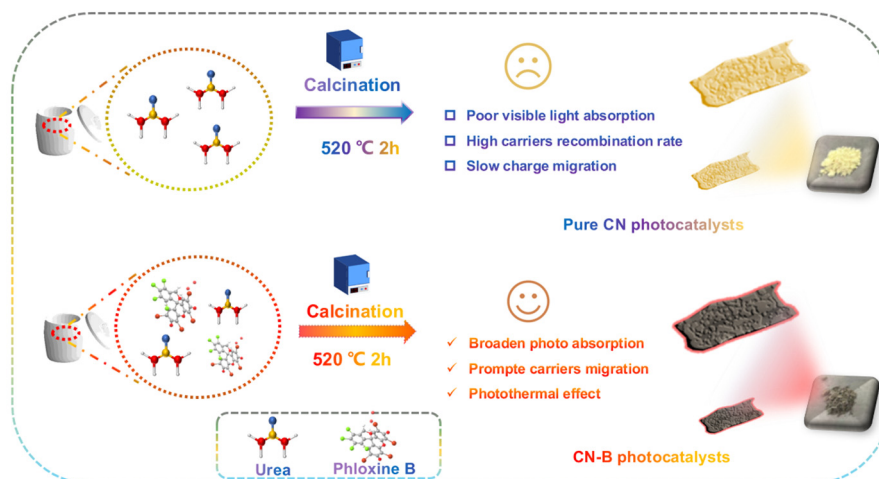
3. Experimental Section

3.1. Materials

The urea ($\text{CO}(\text{NH}_2)_2$) (A.R. $\geq 98\%$) and phloxine B ($\text{C}_{20}\text{H}_2\text{Br}_4\text{Cl}_4\text{Na}_2\text{O}_5$) (A.R. $\geq 80\%$) were purchased from Sinopharm Chemical Reagent Co., Ltd. (Shanghai, China), and were analytical grade without further purification.

3.2. Preparation of CN and CN-B Materials

The black $\text{g-C}_3\text{N}_4$ (CN-B) materials were synthesized by a one-step calcination method with controlling the additional amount of phloxine B powder (Scheme 1). Firstly, X mg ($X = 5, 10, 20,$ and 30) of phloxine B was ground with 10 g of urea in a mortar. Next, after sufficient grinding, the mixture in the mortar was placed in a crucible and heated to 520°C at a heating rate of $5^\circ\text{C}/\text{min}$ under an air atmosphere and maintained for 2 h. Finally, after natural cooling, the resulting powder was washed and dried to obtain CN-B photocatalysts. According to the quality of the phloxine B placed in the precursor before the calcination, the resulting samples were labeled as CN-B-0.05, CN-B-0.1, CN-B-0.2, and CN-B-0.3, respectively. Additionally, the pure CN sample was synthesized under the same reaction conditions except for the addition of phloxine B.



Scheme 1. Schematic diagram of the synthesis process of the pure CN and CN-B nanosheets.

3.3. Photocatalytic Degradation Experiments

The photocatalytic degradation performances of as-prepared samples were evaluated by using a parallel photochemical reaction instrument (CEL-LAB200E7, Beijing Zhongyang Jinyuan Technology Co., LTD., Beijing, China) and 30W LED lamp as vis light source (λ : 410–760 nm). Specifically, a certain amount of photocatalyst powder and TC aqueous solution (50 mL, 30 mg/L) were dispersed into seawater (3.5 wt% NaCl solution) and stirred in the dark for 30 min to achieve adsorption–desorption equilibrium. After the adsorption equilibrium was reached, the LED lamp was opened for 120 min to evaluate the degradation efficiency of CN and CN-B photocatalysts under visible light irradiation. The photocatalytic degradation of TC was detected by UV-Vis spectrophotometer (UV-2450, Shanghai, China) at a maximum wavelength of 357 nm with 20 min intervals; withdrawn samples were extracted from the suspension and centrifuged. In order to test the cyclic degradation stability of the synthesized sample, the photocatalyst, after degradation, was collected by centrifuge and washed and dried for repeated testing. In addition, the solution temperature of the reactor can be controlled by a condensate circulation device to allow photocatalytic degradation experiments to be performed at different temperatures (such as 5 and 10 °C).

The specific experimental procedures of characterizations, photoelectrochemical properties measurements, and photothermal performance measurements were listed in the Supporting Information.

4. Conclusions

In summary, a stable photothermal-assisted photocatalytic degradation TC system was designed, and a black carbon nitride (CN-B) photocatalyst was constructed by one-step calcination of urea and phloxine B. The results showed that the photocatalytic degradation TC in simulated seawater for the optimal sample CN-B-0.1 was 92% within 2 h at room temperature under visible light irradiation. The excellent photocatalytic degradation performance is mainly attributed to the following reasons: (i) the charge transfer distance reduced by the thickness of ultra-thin nanosheets, (ii) the introduction of cyanogen defects promotes photogenerated carrier separation and migration, and (iii) the photothermal effect of CN-B increases the temperature of the reaction system and further improves the photocatalytic degradation performance. This work provides a promising strategy and systematic method for developing g-C₃N₄-based photocatalysts for photothermal-assisted photocatalytic degradation of antibiotics.

Supplementary Materials: The following supporting information can be downloaded at: <https://www.mdpi.com/article/10.3390/catal13071147/s1>, Figure S1. Energy dispersive X-ray spectra (EDX) spectrum of CN-B-0.1 sample. Figure S2. High-resolution XPS spectra of Na 1s for CN and CN-B-0.1 photocatalysts. Figure S3. Digital photos of (a) CN, (b) CN-B-0.05, (c) CN-B-0.1, (d) CN-B-0.3 and (e) CN-B-0.5. Figure S4. Photocatalytic Tc degradation performance of CN-B-0.1 photocatalyst compared with the previously reported of the different materials. Figure S5. High-resolution XPS spectra of O 1s of CN-B-0.1 photocatalyst before and after photocatalysis. Table S1. Surface relative element content of CN and CN-B-0.1 from XPS characterizes. Table S2. Photocatalytic Tc degradation performance of CN-B-0.1 photocatalyst compared with the previously reported of the different materials [72–75].

Author Contributions: Data curation, L.J.N.K. and J.L.; Writing—original draft, L.J.N.K. and Z.C.; Writing—review & editing, H.W., F.G. and W.S. All authors have read and agreed to the published version of the manuscript.

Funding: The authors would like to acknowledge the funding support from the National Natural Science Foundation of China (No. 22006057 and 21908115) and “Doctor of Mass entrepreneurship and innovation” Project in Jiangsu Province.

Data Availability Statement: Samples of the compounds are available or not available from the authors.

Conflicts of Interest: The authors declare no conflict of interest.

References

1. Zheng, D.; Chang, Q.; Gao, M.; She, Z.; Jin, C.; Guo, L.; Zhao, Y.; Wang, S.; Wang, X. Performance evaluation and microbial community of a sequencing batch biofilm reactor (SBBR) treating mariculture wastewater at different chlortetracycline concentrations. *J. Environ. Manag.* **2016**, *182*, 496–504. [[CrossRef](#)] [[PubMed](#)]
2. Liu, X.; Steele, J.C.; Meng, X.Z. Usage, residue, and human health risk of antibiotics in Chinese aquaculture: A review. *Environ. Pollut.* **2017**, *223*, 161–169. [[CrossRef](#)] [[PubMed](#)]
3. Hu, J.; Sun, C.; Wu, L.-X.; Zhao, G.-Q.; Liu, H.-Y.; Jiao, F.-P. Halogen doped g-C₃N₄/ZnAl-LDH hybrid as a Z-scheme photocatalyst for efficient degradation for tetracycline in seawater. *Sep. Purif. Technol.* **2023**, *309*, 123047. [[CrossRef](#)]
4. Zhu, D.; Cai, L.; Sun, Z.; Zhang, A.; Heroux, P.; Kim, H.; Yu, W.; Liu, Y. Efficient degradation of tetracycline by RGO@black titanium dioxide nanofluid via enhanced catalysis and photothermal conversion. *Sci. Total Environ.* **2021**, *787*, 147536. [[CrossRef](#)] [[PubMed](#)]
5. Lu, Z.; Yu, Z.; Dong, J.; Song, M.; Liu, Y.; Liu, X.; Ma, Z.; Su, H.; Yan, Y.; Huo, P. Facile microwave synthesis of a Z-scheme imprinted ZnFe₂O₄/Ag/PEDOT with the specific recognition ability towards improving photocatalytic activity and selectivity for tetracycline. *Chem. Eng. J.* **2018**, *337*, 228–241. [[CrossRef](#)]
6. Lou, J.; Xu, X.; Gao, Y.; Zheng, D.; Wang, J.; Li, Z. Preparation of magnetic activated carbon from waste rice husk for the determination of tetracycline antibiotics in water samples. *RSC Adv.* **2016**, *6*, 112166–112174. [[CrossRef](#)]
7. Sun, H.; Guo, F.; Pan, J.; Huang, W.; Wang, K.; Shi, W. One-pot thermal polymerization route to prepare N-deficient modified g-C₃N₄ for the degradation of tetracycline by the synergistic effect of photocatalysis and persulfate-based advanced oxidation process. *Chem. Eng. J.* **2021**, *406*, 126844. [[CrossRef](#)]
8. Davison, J. Genetic exchange between bacteria in the environment. *Plasmid* **1999**, *42*, 73–91. [[CrossRef](#)]
9. Niu, J.; Lin, H.-Z.; Jiang, S.-G.; Chen, X.; Wu, K.-C.; Liu, Y.-J.; Wang, S.; Tian, L.-X. Comparison of effect of chitin, chitosan, chitosan oligosaccharide and N-acetyl-D-glucosamine on growth performance, antioxidant defenses and oxidative stress status of *Penaeus monodon*. *Aquaculture* **2013**, *372–375*, 1–8. [[CrossRef](#)]
10. Jeong, W.G.; Kim, J.G.; Baek, K. Removal of 1,2-dichloroethane in groundwater using Fenton oxidation. *J. Hazard. Mater.* **2022**, *428*, 128253. [[CrossRef](#)]
11. Liu, Z.; Lompe, K.M.; Mohseni, M.; Berube, P.R.; Sauve, S.; Barbeau, B. Biological ion exchange as an alternative to biological activated carbon for drinking water treatment. *Water Res.* **2020**, *168*, 115148. [[CrossRef](#)]
12. Liu, Y.; Yu, X. Carbon dioxide adsorption properties and adsorption/desorption kinetics of amine-functionalized KIT-6. *Appl. Energy* **2018**, *211*, 1080–1088. [[CrossRef](#)]
13. Guo, F.; Shi, W.; Li, M.; Shi, Y.; Wen, H. 2D/2D Z-scheme heterojunction of CuInS₂/g-C₃N₄ for enhanced visible-light-driven photocatalytic activity towards the degradation of tetracycline. *Sep. Purif. Technol.* **2019**, *210*, 608–615. [[CrossRef](#)]
14. Zhang, T.; Liu, M.; Meng, Y.; Huang, B.; Pu, X.; Shao, X. A novel method for the synthesis of Ag₃VO₄/Ag₂VO₂PO₄ heterojunction photocatalysts with improved visible-light photocatalytic properties. *Sep. Purif. Technol.* **2018**, *206*, 149–157. [[CrossRef](#)]
15. Lu, C.; Guo, F.; Yan, Q.; Zhang, Z.; Li, D.; Wang, L.; Zhou, Y. Hydrothermal synthesis of type II ZnIn₂S₄/BiPO₄ heterojunction photocatalyst with dandelion-like microflower structure for enhanced photocatalytic degradation of tetracycline under simulated solar light. *J. Alloys Compd.* **2019**, *811*, 151976. [[CrossRef](#)]
16. Zu, M.; Zhou, X.; Zhang, S.; Qian, S.; Li, D.-S.; Liu, X.; Zhang, S. Sustainable engineering of TiO₂-based advanced oxidation technologies: From photocatalyst to application devices. *J. Mater. Sci. Technol.* **2021**, *78*, 202–222. [[CrossRef](#)]
17. Qiao, X.; Wang, C.; Niu, Y. N-Benzyl HMTA induced self-assembly of organic-inorganic hybrid materials for efficient photocatalytic degradation of tetracycline. *J. Hazard. Mater.* **2020**, *391*, 122121. [[CrossRef](#)]
18. Reddy, K.R.; Reddy, C.V.; Nadagouda, M.N.; Shetti, N.P.; Jaesool, S.; Aminabhavi, T.M. Polymeric graphitic carbon nitride (g-C₃N₄)-based semiconducting nanostructured materials: Synthesis methods, properties and photocatalytic applications. *J. Environ. Manag.* **2019**, *238*, 25–40. [[CrossRef](#)]
19. Shi, W.; Li, M.; Huang, X.; Ren, H.; Yan, C.; Guo, F. Facile synthesis of 2D/2D Co₃(PO₄)₂/g-C₃N₄ heterojunction for highly photocatalytic overall water splitting under visible light. *Chem. Eng. J.* **2020**, *382*, 122960. [[CrossRef](#)]
20. Shi, W.; Ren, H.; Huang, X.; Li, M.; Tang, Y.; Guo, F. Low cost red mud modified graphitic carbon nitride for the removal of organic pollutants in wastewater by the synergistic effect of adsorption and photocatalysis. *Sep. Purif. Technol.* **2020**, *237*, 116477. [[CrossRef](#)]
21. Mishra, A.; Mehta, A.; Basu, S.; Shetti, N.P.; Reddy, K.R.; Aminabhavi, T.M. Graphitic carbon nitride (g-C₃N₄)-based metal-free photocatalysts for water splitting: A review. *Carbon* **2019**, *149*, 693–721. [[CrossRef](#)]
22. Yu, W.; Shan, X.; Zhao, Z. Unique nitrogen-deficient carbon nitride homojunction prepared by a facile inserting-removing strategy as an efficient photocatalyst for visible light-driven hydrogen evolution. *Appl. Catal. B Environ.* **2020**, *269*, 118778. [[CrossRef](#)]
23. Shi, W.; Shu, K.; Huang, X.; Ren, H.; Li, M.; Chen, F.; Guo, F. Enhancement of visible-light photocatalytic degradation performance over nitrogen-deficient g-C₃N₄/KNbO₃ heterojunction photocatalyst. *J. Chem. Technol. Biotechnol.* **2020**, *95*, 1476–1486. [[CrossRef](#)]
24. Feng, C.; Lu, Z.; Zhang, Y.; Liang, Q.; Zhou, M.; Li, X.; Yao, C.; Li, Z.; Xu, S. A magnetically recyclable dual Z-scheme GCNQDs-CoTiO₃/CoFe₂O₄ composite photocatalyst for efficient photocatalytic degradation of oxytetracycline. *Chem. Eng. J.* **2022**, *435*, 134833. [[CrossRef](#)]
25. Wu, M.; He, X.; Jing, B.; Wang, T.; Wang, C.; Qin, Y.; Ao, Z.; Wang, S.; An, T. Novel carbon and defects co-modified g-C₃N₄ for highly efficient photocatalytic degradation of bisphenol A under visible light. *J. Hazard. Mater.* **2020**, *384*, 121323. [[CrossRef](#)]

26. Li, Y.; Fang, Y.; Cao, Z.; Li, N.; Chen, D.; Xu, Q.; Lu, J. Construction of g-C₃N₄/PDI@MOF heterojunctions for the highly efficient visible light-driven degradation of pharmaceutical and phenolic micropollutants. *Appl. Catal. B Environ.* **2019**, *250*, 150–162. [[CrossRef](#)]
27. Liu, G.; Dong, G.; Zeng, Y.; Wang, C. The photocatalytic performance and active sites of g-C₃N₄ effected by the coordination doping of Fe(III). *Chin. J. Catal.* **2020**, *41*, 1564–1572. [[CrossRef](#)]
28. Hu, X.; Lu, P.; Pan, R.; Li, Y.; Bai, J.; He, Y.; Zhang, C.; Jia, F.; Fu, M. Metal-ion-assisted construction of cyano group defects in g-C₃N₄ to simultaneously degrade wastewater and produce hydrogen. *Chem. Eng. J.* **2021**, *423*, 130278. [[CrossRef](#)]
29. Lu, Y.; Zhang, H.; Fan, D.; Chen, Z.; Yang, X. Coupling solar-driven photothermal effect into photocatalysis for sustainable water treatment. *J. Hazard. Mater.* **2022**, *423*, 127128. [[CrossRef](#)]
30. Yang, X.; Wei, S.; Ma, X.; Gao, Z.; Huang, W.; Wang, D.; Liu, Z.; Wang, J. Core-shell CoTiO₃@MnO₂ heterostructure for the photothermal degradation of tetracycline. *J. Mater. Sci.* **2023**, *58*, 3551–3567. [[CrossRef](#)]
31. Wang, T.; Bai, Z.; Wei, W.; Hou, F.; Guo, W.; Wei, A. beta-Cyclodextrin-Derivative-Functionalized Graphene Oxide/Graphitic Carbon Nitride Composites with a Synergistic Effect for Rapid and Efficient Sterilization. *ACS Appl. Mater. Interfaces* **2022**, *14*, 474–483. [[CrossRef](#)]
32. Zhang, X.; Ma, Y.; Zhang, X.; Pang, X.; Yang, Z. Bio-inspired self-assembled bacteriochlorin nanoparticles for superior visualization and photothermal ablation of tumors. *Biomed. Pharmacother.* **2023**, *165*, 115014. [[CrossRef](#)] [[PubMed](#)]
33. Hou, B.; Shi, Z.; Kong, D.; Chen, Z.; Yang, K.; Ming, X.; Wang, X. Scalable porous Al foil/reduced graphene oxide/Mn₃O₄ composites for efficient fresh water generation. *Mater. Today Energy* **2020**, *15*, 100371. [[CrossRef](#)]
34. Wang, Y.; Yang, W.; Chen, X.; Wang, J.; Zhu, Y. Photocatalytic activity enhancement of core-shell structure g-C₃N₄@TiO₂ via controlled ultrathin g-C₃N₄ layer. *Appl. Catal. B Environ.* **2018**, *220*, 337–347. [[CrossRef](#)]
35. Guo, F.; Sun, H.; Huang, X.; Shi, W.; Yan, C. Fabrication of TiO₂/high-crystalline g-C₃N₄ composite with enhanced visible-light photocatalytic performance for tetracycline degradation. *J. Chem. Technol. Biotechnol.* **2020**, *95*, 2684–2693. [[CrossRef](#)]
36. Tan, X.; Jiang, K.; Zhai, S.; Zhou, J.; Wang, J.; Cadien, K.; Li, Z. X-Ray Spectromicroscopy Investigation of Heterogeneous Sodiation in Hard Carbon Nanosheets with Vertically Oriented (002) Planes. *Small* **2021**, *17*, e2102109. [[CrossRef](#)]
37. Guo, F.; Wang, L.; Sun, H.; Li, M.; Shi, W. High-efficiency photocatalytic water splitting by a N-doped porous g-C₃N₄ nanosheet polymer photocatalyst derived from urea and N,N-dimethylformamide. *Inorg. Chem. Front.* **2020**, *7*, 1770–1779. [[CrossRef](#)]
38. Jin, W.; Ji, Y.; Larsen, D.H.; Huang, Y.; Heuvelink, E.; Marcelis, L.F.M. Gradually increasing light intensity during the growth period increases dry weight production compared to constant or gradually decreasing light intensity in lettuce. *Sci. Hortic.* **2023**, *311*, 111807. [[CrossRef](#)]
39. Shi, Y.; Li, L.; Sun, H.; Xu, Z.; Cai, Y.; Shi, W.; Guo, F.; Du, X. Engineering ultrathin oxygen-doped g-C₃N₄ nanosheet for boosted photoredox catalytic activity based on a facile thermal gas-shocking exfoliation effect. *Sep. Purif. Technol.* **2022**, *292*, 121038. [[CrossRef](#)]
40. Shi, W.; Shu, K.; Sun, H.; Ren, H.; Li, M.; Chen, F.; Guo, F. Dual enhancement of capturing photogenerated electrons by loading CoP nanoparticles on N-deficient graphitic carbon nitride for efficient photocatalytic degradation of tetracycline under visible light. *Sep. Purif. Technol.* **2020**, *246*, 116930. [[CrossRef](#)]
41. Wang, J.; Huang, J.; Xie, H.; Qu, A. Synthesis of g-C₃N₄/TiO₂ with enhanced photocatalytic activity for H₂ evolution by a simple method. *Int. J. Hydrogen Energy* **2014**, *39*, 6354–6363. [[CrossRef](#)]
42. Guo, F.; Huang, X.; Chen, Z.; Sun, H.; Chen, L. Prominent co-catalytic effect of CoP nanoparticles anchored on high-crystalline g-C₃N₄ nanosheets for enhanced visible-light photocatalytic degradation of tetracycline in wastewater. *Chem. Eng. J.* **2020**, *395*, 125118. [[CrossRef](#)]
43. Guo, F.; Li, M.; Ren, H.; Huang, X.; Shu, K.; Shi, W.; Lu, C. Facile bottom-up preparation of Cl-doped porous g-C₃N₄ nanosheets for enhanced photocatalytic degradation of tetracycline under visible light. *Sep. Purif. Technol.* **2019**, *228*, 115770. [[CrossRef](#)]
44. Guo, F.; Wang, L.; Sun, H.; Li, M.; Shi, W.; Lin, X. A one-pot sealed ammonia self-etching strategy to synthesis of N-defective g-C₃N₄ for enhanced visible-light photocatalytic hydrogen. *Int. J. Hydrogen Energy* **2020**, *45*, 30521–30532. [[CrossRef](#)]
45. Zeng, D.; Ong, W.-J.; Chen, Y.; Tee, S.Y.; Chua, C.S.; Peng, D.-L.; Han, M.-Y. Co₂P Nanorods as an Efficient Cocatalyst Decorated Porous g-C₃N₄ Nanosheets for Photocatalytic Hydrogen Production under Visible Light Irradiation. *Part. Part. Syst. Charact.* **2018**, *35*, 1700251. [[CrossRef](#)]
46. Shi, W.; Yang, S.; Sun, H.; Wang, J.; Lin, X.; Guo, F.; Shi, J. Carbon dots anchored high-crystalline g-C₃N₄ as a metal-free composite photocatalyst for boosted photocatalytic degradation of tetracycline under visible light. *J. Mater. Sci.* **2020**, *56*, 2226–2240. [[CrossRef](#)]
47. Guo, S.; Deng, Z.; Li, M.; Jiang, B.; Tian, C.; Pan, Q.; Fu, H. Phosphorus-Doped Carbon Nitride Tubes with a Layered Micro-nanostructure for Enhanced Visible-Light Photocatalytic Hydrogen Evolution. *Angew. Chem. Int. Ed. Engl.* **2016**, *55*, 1830–1834. [[CrossRef](#)] [[PubMed](#)]
48. Zhu, X.; Guo, F.; Pan, J.; Sun, H.; Gao, L.; Deng, J.; Zhu, X.; Shi, W. Fabrication of visible-light-response face-contact ZnSnO₃@g-C₃N₄ core-shell heterojunction for highly efficient photocatalytic degradation of tetracycline contaminant and mechanism insight. *J. Mater. Sci.* **2020**, *56*, 4366–4379. [[CrossRef](#)]
49. Qin, J.; Chen, J.; Salisbury, J.B. Photon transferred TL signals from potassium feldspars and their effects on post-IR IRSL measurements. *J. Lumin.* **2015**, *160*, 1–8. [[CrossRef](#)]

50. Guo, F.; Huang, X.; Chen, Z.; Cao, L.; Cheng, X.; Chen, L.; Shi, W. Construction of Cu₃P-ZnSnO₃-g-C₃N₄ p-n-n heterojunction with multiple built-in electric fields for effectively boosting visible-light photocatalytic degradation of broad-spectrum antibiotics. *Sep. Purif. Technol.* **2021**, *265*, 118477. [[CrossRef](#)]
51. Fu, J.; Zhu, B.; Jiang, C.; Cheng, B.; You, W.; Yu, J. Hierarchical Porous O-Doped g-C₃N₄ with Enhanced Photocatalytic CO₂ Reduction Activity. *Small* **2017**, *13*, 1603938. [[CrossRef](#)] [[PubMed](#)]
52. Zhang, W.; Shi, W.; Sun, H.; Shi, Y.; Luo, H.; Jing, S.; Fan, Y.; Guo, F.; Lu, C. Fabrication of ternary CoO/g-C₃N₄/Co₃O₄ nanocomposite with p-n-p type heterojunction for boosted visible-light photocatalytic performance. *J. Chem. Technol. Biotechnol.* **2021**, *96*, 1854–1863. [[CrossRef](#)]
53. Liu, G.; Yan, S.; Shi, L.; Yao, L. The Improvement of Photocatalysis H₂ Evolution Over g-C₃N₄ With Na and Cyano-Group Co-modification. *Front. Chem.* **2019**, *7*, 639. [[CrossRef](#)]
54. Guo, F.; Chen, Z.; Huang, X.; Cao, L.; Cheng, X.; Shi, W.; Chen, L. Cu₃P nanoparticles decorated hollow tubular carbon nitride as a superior photocatalyst for photodegradation of tetracycline under visible light. *Sep. Purif. Technol.* **2021**, *275*, 119223. [[CrossRef](#)]
55. Chen, H.; Yu, Y.; Yu, Y.; Ye, J.; Zhang, S.; Chen, J. Exogenous electron transfer mediator enhancing gaseous toluene degradation in a microbial fuel cell: Performance and electron transfer mechanism. *Chemosphere* **2021**, *282*, 131028. [[CrossRef](#)]
56. Shi, Y.; Li, L.; Xu, Z.; Sun, H.; Guo, F.; Shi, W. One-step simple green method to prepare carbon-doped graphitic carbon nitride nanosheets for boosting visible-light photocatalytic degradation of tetracycline. *J. Chem. Technol. Biotechnol.* **2021**, *96*, 3122–3133. [[CrossRef](#)]
57. Guo, F.; Chen, Z.; Huang, X.; Cao, L.; Cheng, X.; Shi, W.; Chen, L. Ternary Ni₂P/Bi₂MoO₆/g-C₃N₄ composite with Z-scheme electron transfer path for enhanced removal broad-spectrum antibiotics by the synergistic effect of adsorption and photocatalysis. *Chin. J. Chem. Eng.* **2022**, *44*, 157–168. [[CrossRef](#)]
58. Xu, Z.; Shi, Y.; Li, L.; Sun, H.; Amin, M.D.S.; Guo, F.; Wen, H.; Shi, W. Fabrication of 2D/2D Z-scheme highly crystalline carbon nitride/ δ -Bi₂O₃ heterojunction photocatalyst with enhanced photocatalytic degradation of tetracycline. *J. Alloys Compd.* **2022**, *895*, 162667. [[CrossRef](#)]
59. Liu, Y.; Yang, Z.-H.; Song, P.-P.; Xu, R.; Wang, H. Facile synthesis of Bi₂MoO₆/ZnSnO₃ heterojunction with enhanced visible light photocatalytic degradation of methylene blue. *Appl. Surf. Sci.* **2018**, *430*, 561–570. [[CrossRef](#)]
60. Cheng, Q.; Yang, W.; Chen, Q.; Zhu, J.; Li, D.; Fu, L.; Zhou, L. Fe-doped zirconia nanoparticles with highly negative conduction band potential for enhancing visible light photocatalytic performance. *Appl. Surf. Sci.* **2020**, *530*, 147291. [[CrossRef](#)]
61. Sun, H.; Wang, L.; Guo, F.; Shi, Y.; Li, L.; Xu, Z.; Yan, X.; Shi, W. Fe-doped g-C₃N₄ derived from biowaste material with Fe-N bonds for enhanced synergistic effect between photocatalysis and Fenton degradation activity in a broad pH range. *J. Alloys Compd.* **2022**, *900*, 163410. [[CrossRef](#)]
62. Guo, F.; Chen, Z.; Shi, Y.; Cao, L.; Cheng, X.; Shi, W.; Chen, L.; Lin, X. A ragged porous hollow tubular carbon nitride towards boosting visible-light photocatalytic hydrogen production in water and seawater. *Renew. Energy* **2022**, *188*, 1–10. [[CrossRef](#)]
63. Shi, Y.; Li, L.; Xu, Z.; Sun, H.; Amin, S.; Guo, F.; Shi, W.; Li, Y. Engineering of 2D/3D architectures type II heterojunction with high-crystalline g-C₃N₄ nanosheets on yolk-shell ZnFe₂O₄ for enhanced photocatalytic tetracycline degradation. *Mater. Res. Bull.* **2022**, *150*, 111789. [[CrossRef](#)]
64. Sun, H.; Shi, Y.; Shi, W.; Guo, F. High-crystalline/amorphous g-C₃N₄ S-scheme homojunction for boosted photocatalytic H₂ production in water/simulated seawater: Interfacial charge transfer and mechanism insight. *Appl. Surf. Sci.* **2022**, *593*, 153281. [[CrossRef](#)]
65. Sun, X.; Shi, Y.; Lu, J.; Shi, W.; Guo, F. Template-free self-assembly of three-dimensional porous graphitic carbon nitride nanovesicles with size-dependent photocatalytic activity for hydrogen evolution. *Appl. Surf. Sci.* **2022**, *606*, 154841. [[CrossRef](#)]
66. Shi, W.; Cao, L.; Shi, Y.; Chen, Z.; Cai, Y.; Guo, F.; Du, X. Environmentally friendly supermolecule self-assembly preparation of S-doped hollow porous tubular g-C₃N₄ for boosted photocatalytic H₂ production. *Ceram. Int.* **2023**, *49*, 11989–11998. [[CrossRef](#)]
67. Shi, Y.; Li, L.; Xu, Z.; Guo, F.; Li, Y.; Shi, W. Synergistic coupling of piezoelectric and plasmonic effects regulates the Schottky barrier in Ag nanoparticles/ultrathin g-C₃N₄ nanosheets heterostructure to enhance the photocatalytic activity. *Appl. Surf. Sci.* **2023**, *616*, 156466. [[CrossRef](#)]
68. Guo, F.; Li, L.; Shi, Y.; Shi, W.; Yang, X. Synthesis of N-deficient g-C₃N₄/epoxy composite coating for enhanced photocatalytic corrosion resistance and water purification. *J. Mater. Sci.* **2023**, *58*, 4223–4239. [[CrossRef](#)]
69. Guo, F.; Li, L.; Shi, Y.; Shi, W.; Yang, X.; Li, H. Achieving superior anticorrosion and antibiofouling performance of polyaniline/graphitic carbon nitride composite coating. *Progress. Org. Coat.* **2023**, *179*, 107512. [[CrossRef](#)]
70. Li, L.; Zhang, Y.; Shi, Y.; Guo, F.; Yang, X.; Shi, W. A hydrophobic high-crystalline g-C₃N₄/epoxy resin composite coating with excellent durability and stability for long-term corrosion resistance. *Mater. Today Commun.* **2023**, *35*, 105692. [[CrossRef](#)]
71. Yuan, H.; Sun, H.; Shi, Y.; Wang, J.; Bian, A.; Hu, Y.; Guo, F.; Shi, W.; Du, X.; Kang, Z. Cooperation of carbon doping and carbon loading boosts photocatalytic activity by the optimum photo-induced electron trapping and interfacial charge transfer. *Chem. Eng. J.* **2023**, *472*, 144654. [[CrossRef](#)]
72. Xu, W.; Lai, S.; Pillai, S.C.; Chu, W.; Hu, Y.; Jiang, X.; Fu, M.; Wu, X.; Li, F.; Wang, H. Visible light photocatalytic degradation of tetracycline with porous Ag/graphite carbon nitride plasmonic composite: Degradation pathways and mechanism. *J. Colloid Interface Sci.* **2020**, *574*, 110–121. [[CrossRef](#)] [[PubMed](#)]

73. Hernandez-Uresti, D.B.; Vazquez, A.; Sanchez-Martinez, D.; Obregon, S. Performance of the polymeric g-C₃N₄ photocatalyst through the degradation of pharmaceutical pollutants under UV-vis irradiation. *J. Photo Chem. Photo Biol. A* **2016**, *324*, 47–52. [[CrossRef](#)]
74. Hong, Y.; Li, C.; Zhang, G.; Meng, Y.; Yin, B.; Zhao, Y.; Shi, W. Efficient and stable Nb₂O₅ modified g-C₃N₄ photocatalyst for removal of antibiotic pollutant. *Chem. Eng. J.* **2016**, *299*, 74–84. [[CrossRef](#)]
75. Chen, D.; Wu, S.; Fang, J.; Lu, S.; Zhou, G.; Feng, W.; Yang, F.; Chen, Y.; Fang, Z. A nanosheet-like α-Bi₂O₃/g-C₃N₄ heterostructure modified by plasmonic metallic Bi and oxygen vacancies with high photodegradation activity of organic pollutants. *Sep. Purif. Technol.* **2018**, *193*, 232–241. [[CrossRef](#)]

Disclaimer/Publisher's Note: The statements, opinions and data contained in all publications are solely those of the individual author(s) and contributor(s) and not of MDPI and/or the editor(s). MDPI and/or the editor(s) disclaim responsibility for any injury to people or property resulting from any ideas, methods, instructions or products referred to in the content.